Physics of Semiconductors.
Solid state physics

UDC 538.915:538.95

EDN SOAOFH
https://www.doi.org/10.33910/2687-153X-2026-7-1-3-15

SERS effect on the surface of ZnO nanorods coated with $CsPbBr_3$

V. A. Gushchina ✉[1], E. P. Averochkin [2], M. A. Teplonogova [1], E. A. Lebedev [2], S. A. Kozyukhin [1]

[1] Kurnakov Institute of General and Inorganic Chemistry of the Russian Academy of Sciences (IGIC RAS),
31 Leninsky Prospekt, Moscow 119991, Russia
[2] National Research University of Electronic Technology (MIET),
1 Shokin Square, Zelenograd, Moscow 124498, Russia

Authors

Valeriya A. Gushchina, ORCID: 0009-0008-9530-1864, e-mail: ya.l2er0us0ya2012@yandex.ru

Evgenii P. Averochkin, ORCID: 0009-0003-4543-3045, e-mail: aep1997@rambler.ru

Maria A. Teplonogova, ORCID: 0000-0002-4820-8498, e-mail: ma_teplonogova@igic.ras.ru

Egor A. Lebedev, ORCID: 0000-0002-5085-5408, e-mail: dr.beefheart@gmail.com

Sergei A. Kozyukhin, ORCID: 0000-0002-7405-551X, e-mail: sergkoz@igic.ras.ru

For citation: Gushchina, V. A., Averochkin, E. P., Teplonogova, M. A., Lebedev, E. A., Kozyukhin, S. A. (2026) SERS effect on the surface of ZnO nanorods coated with $CsPbBr_3$. *Physics of Complex Systems*, 7 (1), 3–15. https://www.doi.org/10.33910/2687-153X-2026-7-1-3-15 EDN SOAOFH

Received 11 December 2025; reviewed 19 January 2026; accepted 20 January 2026.

Funding: The study did not receive any external funding.

Abstract. Heterostructures based on ZnO nanorods and $CsPbBr_3$ nanocrystals were investigated for their potential as semiconductor SERS substrates. We found that ZnO morphology governs the efficiency of interfacial energy transfer, leading to enhanced photoluminescence under 390 nm excitation and a noticeable reduction of the bandgap in the composites. Raman analysis revealed a pronounced intensity enhancement and the emergence of low-frequency $CsPbBr_3$ modes isolated via Gaussian deconvolution, which confirms the SERS-like behavior of the hybrid structures. Our results highlight the strong prospects of ZnO/$CsPbBr_3$ heterostructures for sensing and optoelectronic applications.

Keywords: ZnO nanorods, $CsPbBr_3$ quantum dots, SERS effect, Raman enhancement, heterostructures, energy transfer, low-frequency phonons

Introduction

Over the past decades, rapid development of nanotechnology has opened new avenues in spectroscopy, among which Surface-Enhanced Raman Spectroscopy (SERS) features prominently. Based on the resonant enhancement of the Raman scattering cross-section from molecules adsorbed on metallic nanostructures, this method enables detection limits down to the single-molecule level. For instance, in the case of certain dye molecules adsorbed onto silver colloidal clusters, SERS can provide true single-molecule sensitivity. Moreover, local enhancement factors in specific regions ('hot spots') of metallic clusters can reach values on the order of 10^{10}–10^{12} (Yi et al. 2025). SERS has found widespread application in biomedicine, chemical sensing, photocatalysis, nanolaser technology, and materials science due to its ability to provide detailed information about the chemical composition and structural features of analytes (Ahmed et al. 2019; Kim et al. 2008; Sharma et al. 2012; Vo-Dinh et al. 2015; Song et al. 2022). The central component of the SERS effect is the nanostructured surface, which enables both electromagnetic and chemical enhancement of the Raman signal. The electromagnetic contribution arises from

the intense optical near-field generated in the vicinity of the nanostructure as a result of the resonant excitation of localized surface plasmon oscillations in metallic clusters, which strongly amplifies the Raman response of nearby molecules. The parameters of plasmon resonance excitation and the magnitude of near-field enhancement are governed by the morphology of the nanostructure, the electronic conductivity of the metal, and the dielectric properties of the surrounding medium. Traditionally, noble-metal nanostructures — such as gold and silver nanoparticles — serve as SERS-active substrates, where localized surface plasmon resonances (LSPR) generate electromagnetic 'hot spots' with highly amplified optical fields. For isolated spherical silver nanoparticles, the plasmon resonance typically lies in the ~350–450 nm range, and the corresponding electromagnetic enhancement factors of SERS reach values on the order of 10^6–10^7 (Jin et al. 2016; Xu et al. 2025).

For the adsorbate located in direct contact with the metal surface, an additional SERS enhancement mechanism may arise from the coupling between the molecular electronic orbitals and the conduction-band states of the metal. This phenomenon is referred to as the chemical enhancement mechanism, or, alternatively, first-layer enhancement. The contribution of chemical enhancement is not universal, as it strongly depends on the molecular species and its chemical affinity to the metal surface. The magnitude of this mechanism is generally estimated to be no more than two orders of magnitude (Xia et al. 2014; Zhou et al 2025).

A search for nanostructured materials that can serve as alternatives to gold and silver — while offering lower cost, greater stability, and broader multifunctionality — has stimulated active research into semiconductor nanostructures, including ZnO (Kumar et al. 2021) and perovskite materials such as $CsPbBr_3$ (Wang et al. 2023; Wang et al. 2025).

Zinc oxide, a wide-bandgap semiconductor with an energy gap of approximately 3.3–3.7 eV, has long attracted significant research interest due to its unique optical, electronic, and structural properties. ZnO can adopt a wide variety of morphologies, including nanoparticles, nanorods, nanoneedles, nanocages, and nanoflowers (Averochkin et al. 2024; Deng et al. 2009; Djurisic et al. 2012; Majee et al. 2020; Sinha et al. 2011), which makes it a versatile material for applications in solar energy conversion, optoelectronics, biomedicine, and chemical sensing. These structures also exhibit high biocompatibility, pronounced photocatalytic activity, and excellent chemical stability (Kim et al. 2014; Kumar et al. 2017; Samanta, Bandyopadhyay 2012; Shah 2008). In the context of SERS, ZnO exhibits a strong potential both as an independent nanomaterial and as a component in hybrid systems with noble metals. Electromagnetic enhancement in ZnO-based semiconductor structures arises from plasmonic resonances associated with transitions in the valence and conduction bands; however, this enhancement is considerably weaker than that observed in metals, with the corresponding LSPR features typically located in the UV and near-IR spectral regions (Han et al. 2017). To enhance this effect, ZnO is often combined with metals such as Au or Ag (Chiu et al 2018; Dubkov et al. 2024; Novikov et al. 2021), which shifts the LSPR features into the visible spectral range and facilitates the formation of electromagnetic 'hot spots' through interparticle coupling effects.

Another promising alternative is a class of fully inorganic perovskites of the $CsPbX_3$ type (X = Br, Cl, I), which exhibit exceptional optical properties, including high charge-carrier mobility, bright photoluminescence in the visible range, and a tunable bandgap (Djurisic et al. 2012; Wang et al. 2023; Wang et al. 2025). Fully inorganic perovskites are generally more stable than their hybrid organic–inorganic counterparts, in which the organic cation (e. g., methylammonium, MA^+) is replaced by Cs^+ (Gushchina et al. 2024). Their optical characteristics, including absorption and photoluminescence, strongly depend on composition and nanocrystal size, with bandgap energies ranging from 1.68 to 3.25 eV for $CsPbBr_3$, $CsPbCl_3$, and $CsPbI_3$, respectively (Lee et al. 2025; Miao et al. 2025; Zhao et al. 2023).

Combining ZnO nanorods with $CsPbBr_3$ offers new opportunities for SERS. By integrating a ZnO nanorod surface with a layer of perovskite nanocrystals, it is possible to create heterostructures with enhanced interfacial charge transfer. Such systems enable a simultaneous realization of strong electromagnetic enhancement and additional charge-transfer — mediated (chemical) amplification — while also allowing control over molecular selectivity, since electronic interactions may arise between the analyte molecule and the substrate (Alagurasu et al. 2025). This interaction manifests itself in Fermi-level alignment and the formation of intermediate states that facilitate charge transfer upon excitation. Such processes provide an additional chemical contribution to the overall SERS enhancement, potentially increasing the signal intensity by one to two orders of magnitude beyond that achievable through purely electromagnetic mechanisms (Majumdar et al. 2024). In this context, potential 'hot spots' may arise at the ZnO + $CsPbBr_3$ interface due to defect-induced states in the ZnO nanorods

 https://www.doi.org/10.33910/2687-153X-2026-7-1-3-15

(Wu et al. 2019) or resonance phenomena occurring between the coupled layers (Saran et al. 2017; Toma et al. 2025).

The aim of this work is to fabricate ZnO + $CsPbBr_3$ heterostructures, study their optical properties (optical transmittance and photoluminescence), examine the SERS response, and determine the key parameters governing their enhancement behavior.

Experiment

Reagents. Cs_2CO_3 (99.9%, Sigma-Aldrich), $PbBr_2$ (99.999%, Sigma-Aldrich), oleic acid (OA, 97.4%, Ruskhim), oleylamine (OLA, 98%, Sigma-Aldrich), mineral oil (VM-5c, FOXY), and toluene (reagent grade, Khimmed) were used without further purification. Glass substrates coated with fluorine-doped SnO_2 (FTO, Sigma-Aldrich), hydrogen peroxide (H_2O_2, analytical grade, Ruskhim), H_2SO_4 (high purity grade, Ruskhim), C_3H_8O (reagent grade, Khimmed), $Zn(NO_3)_2{\cdot}6H_2O$ (chemically pure grade, Ruskhim), and NaOH (chemically pure grade, Ruskhim) were also employed.

The suspensions were purified using a Sigma 3-30 KS centrifuge operated at 2,000 and 15,000 rpm.

Surface and fracture images of the samples were obtained using a Tescan Amber GMH scanning electron microscope (SEM). SEM micrographs were acquired with Everhart–Thornley secondary electron detectors and a backscattered electron detector at magnifications of ×1,000–300,000 and an accelerating voltage of 1–10 kV.

Absorption spectra of the colloidal solutions were recorded using a dual-beam Cary 5000 spectrophotometer with a spectral resolution of 0.05 nm. Photoluminescence (PL) spectra were collected at room temperature using a single-beam PerkinElmer LS-55 spectrofluorometer (0.5 nm resolution) in the emission range of 350–600 nm, with excitation wavelengths varied from 300 to 420 nm. The slit widths were set to 5 nm.

Electronic absorption spectra of the colloidal dispersions were acquired using a dual-beam Cary 5000 spectrophotometer, operating at a spectral resolution of 0.05 nm. Steady-state photoluminescence measurements were performed at ambient conditions on a PerkinElmer LS-55 spectrofluorometer (0.5 nm resolution). Emission spectra were collected over the 350–600 nm range, while the excitation wavelength was systematically varied between 300 and 420 nm. Both excitation and emission monochromators were set to a slit width of 5 nm to ensure a well-defined spectral bandwidth and high signal fidelity.

Raman spectra were recorded using a 3D scanning confocal Raman microscope (Confotec NR500, SOL Instruments) with a laser $\lambda = 633$ nm. The spectra were collected in the 50–600 cm^{-1} range using a 600 grooves/mm diffraction grating. A 20× / 0.45 NA dry objective was used for focusing. Signal detection was performed with a PROSCAN CCD detector (16 bit, 2048 × 122 pixels) cooled to −25 °C. The spectra were acquired with an exposure time of 2 s and a single accumulation.

Synthesis of $CsPbBr_3$. A mixture containing Cs_2CO_3 (0.6 mmol), mineral oil (10 mL), and oleic acid (0.625 mL) was loaded into a 50-mL three-neck flask. The suspension was heated to 150 °C under Ar atmosphere with magnetic stirring (500 rpm) until complete reaction of cesium carbonate with oleic acid, yielding a clear brown solution. Separately, $PbBr_2$ (1 g, 2.7 mmol) was combined with mineral oil (20 mL) in another three-neck flask. The mixture was degassed under vacuum (10^{-2} mbar) with continuous stirring (1,000 rpm) and subsequently heated to 160 °C for 1 h. Oleic acid (2 mL) and oleylamine (2 mL) were then added, and once the solution became fully transparent (≈15 min), 6 mL of Cs-oleate was swiftly injected, followed by immediate quenching in an ice bath.

The resulting dispersion was centrifuged at 15,000 rpm for 5 min. Ethyl acetate (EA) was added to induce precipitation, and the mixture was transferred into cuvettes and sonicated for 10 min. The suspension was centrifuged again (15,000 rpm, 5 min), the supernatant removed, and the precipitate redispersed in EA:toluene (2:1), followed by an additional 10-min sonication. The precipitation–centrifugation cycle was repeated twice with EA:toluene ratios of 1:1 and 1:2. The final product was dispersed in toluene, sonicated for 10 min, and centrifuged at 2,000 rpm for 5 min to remove large aggregates. The obtained colloidal solution exhibited bright green photoluminescence.

Synthesis of ZnO Nanorods. FTO-coated glass substrates were first cleaned in a 1:1 mixture of H_2O_2 and H_2SO_4 for 20 min. After cleaning, the substrates were sequentially rinsed with hot and cold deionized water and dried in isopropanol vapor. A chemically resistant lacquer was then applied to the FTO surface. ZnO seed layers were deposited by magnetron sputtering for 20 min at a power of 500 W, with the resulting film thickness varying between the samples. Argon was used as the working gas. Prior to deposition, the substrate surfaces underwent ion cleaning for 2 min. After sputtering, the lacquer

layer was removed mechanically. For the hydrothermal growth precursor solution, $Zn(NO_3)_2 \cdot 6H_2O$ (0.74 g) and NaOH (3.98 g) were dissolved in 250 mL of deionized water at room temperature under stirring at 1,000 rpm for 10 min. The solution was then heated to 80 °C for 10 min. Substrates bearing the ZnO seed layer were immersed face-down into the solution for 30–120 min, depending on the desired nanorod length. During growth, the solution was stirred at 800 rpm. The initial pH of each reaction batch was 13. All syntheses were carried out under ambient pressure. After growth, the ZnO nanorod arrays were rinsed with deionized water and dried at room temperature under a stream of compressed air.

Results and Discussion

Four samples (Fig. 1) were investigated, each of them differing in the morphological parameters of the ZnO nanorods (Table 1), which were grown on FTO-coated substrates and subsequently coated with a layer of $CsPbBr_3$ quantum dots. The diagram illustrates the multilayer architecture of the FTO/ZnO NRs/$CsPbBr_3$ heterostructure, accompanied by TEM images of the perovskite nanocrystals and SEM micrographs of the nanorod arrays.

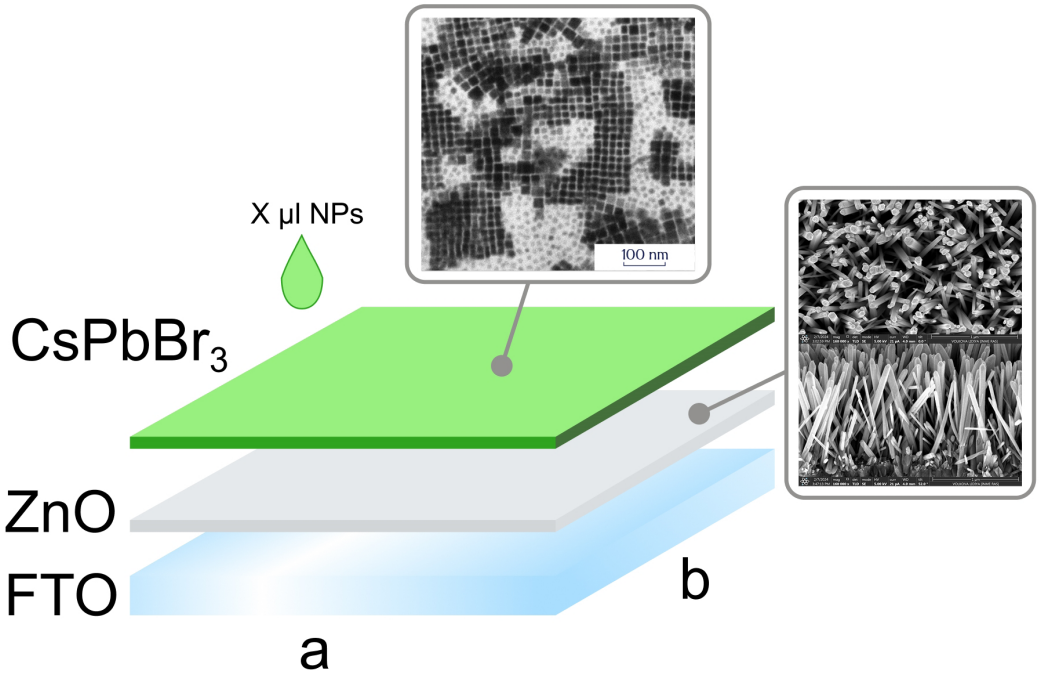

Fig. 1. Diagram of the FTO/ZnO/$CsPbBr_3$ heterostructure

Table 1. Description of the samples

Sample	H NRs, µm	S a. l., mm²	V $CsPbBr_3$, µl
ZnO + $CsPbBr_3$ (1)	1.6 ± 0.1	100	22
ZnO + $CsPbBr_3$ (2)	2.4 ± 0.1	225	50
ZnO + $CsPbBr_3$ (3)	2.7 ± 0.1	192	43

Fig. 2 presents SEM images of ZnO nanorod arrays with various morphologies and corresponding coatings of $CsPbBr_3$ nanoparticles (NPs). Samples a–b serve as references and display a dense, vertically aligned array of pristine ZnO NRs, whereas samples c–h differ in nanorod height (1.6–2.7 µm), which affects the degree of inter-rod filling and the surface coverage density of the deposited perovskite NPs, clearly visible in the top-view images. Cross-sectional views (b, d, f, h) confirm the vertical alignment and thickness variations of the arrays, as well as the distribution of $CsPbBr_3$ across the surfaces and side facets of the nanorods — an important factor for subsequent analysis of the optical and photoelectronic properties of the composite systems.

https://www.doi.org/10.33910/2687-153X-2026-7-1-3-15

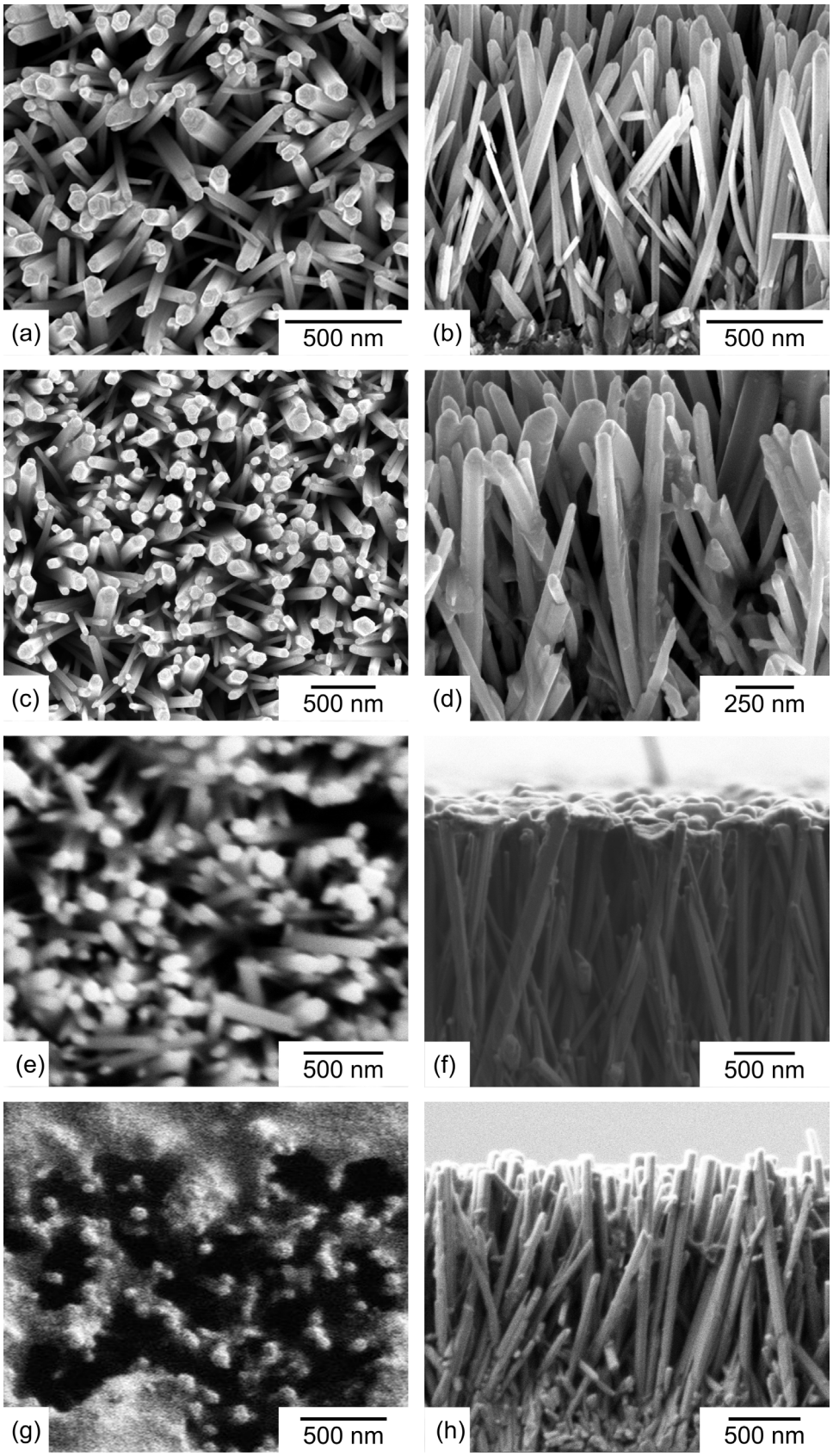

Fig. 2. SEM images of the nanorods and the deposited $CsPbBr_3$: a — ZnO NRs; b — ZnO NRs (fracture); c — 1; d — 1 (fracture); e — 2; f — 2 (fracture); g — 3; h — 3 (fracture)

Across all the three systems (Fig. 3), the ZnO NRs + $CsPbBr_3$ NPs heterostructures exhibit the highest optical density. This enhancement arises from the combined contribution of three factors: an increased effective thickness of the absorbing layer resulting from the incorporation of perovskite NPs into the dense ZnO NR array (Wang et al. 2020); multiple scattering and an extended optical path within the vertically aligned ZnO NRs, which guide and confine the incident radiation (Salem et al. 2025); and the formation of interfacial electronic states at the ZnO + $CsPbBr_3$, which promote stronger absorption and more efficient energy transfer (Peng et al. 2023). Together, these mechanisms lead to an absorption response in the composites that significantly surpasses that of both pristine ZnO NRs and isolated perovskite NPs.

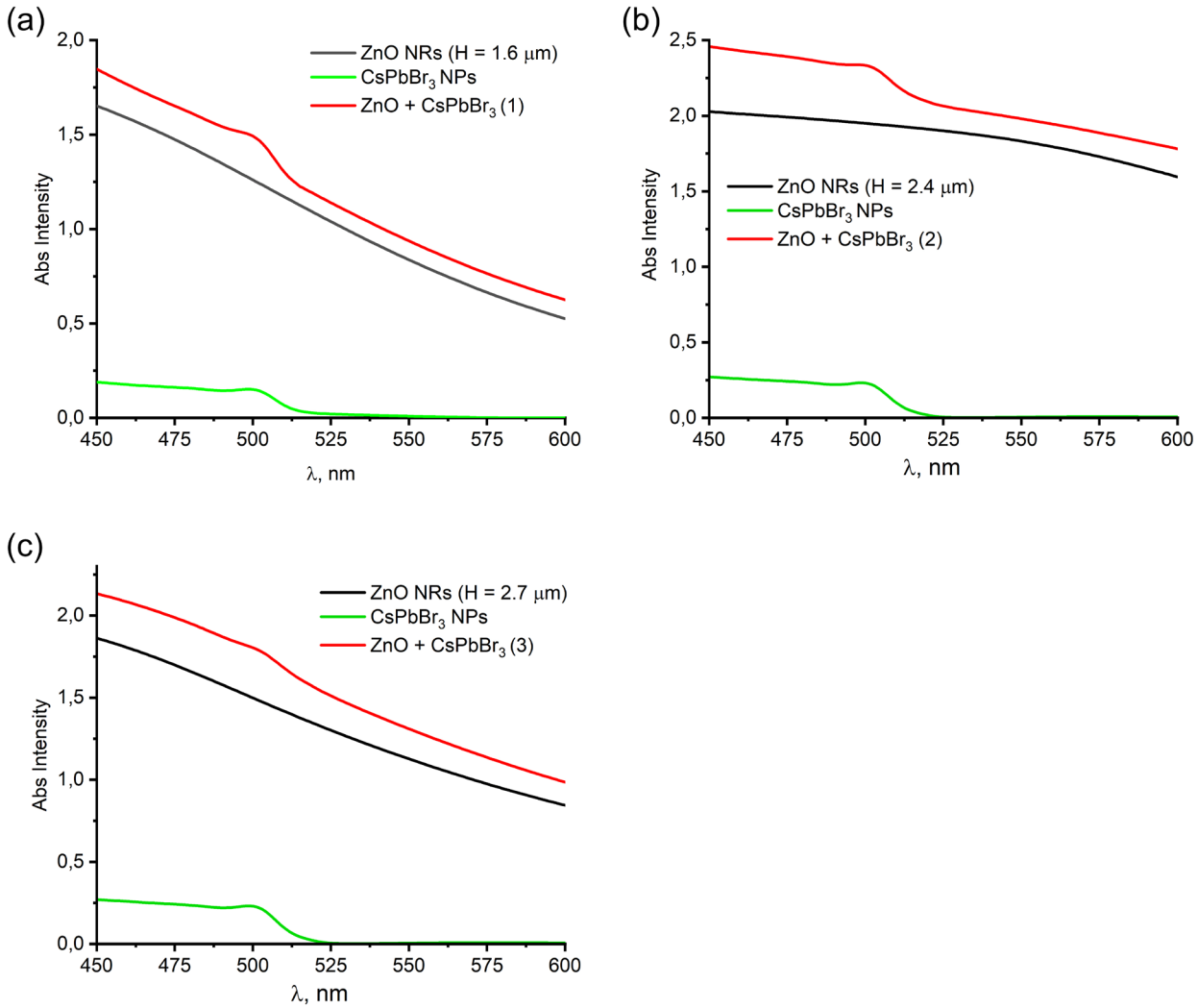

Fig. 3. Absorption spectra of the samples: a — 1 (H = 1.6 μm); b — 2 (H = 2.4 μm); c — 3 (H = 2.7 μm)

The normalized spectra near the absorption edge (Fig. 4) exhibit a characteristic direct band-gap transition with a linear region in the range of ~2.1–2.5 eV. The optical bandgap of the samples was evaluated using the Tauc relation (Tauc, Scott 1967):

$$(\alpha h\nu)^n = B \cdot (h\nu - E_g),$$

where α is the absorption coefficient, h is Planck's constant (6.626×10^{-34} $m^2 \cdot kg \cdot s^{-1}$), ν is the photon frequency, n is the exponent determined by the nature of the electronic transition, and E_g is the optical bandgap energy. Since both ZnO and $CsPbBr_3$ are direct-bandgap semiconductors, the appropriate exponent in this case is n = 2 (Coulter, Birnie 2018).

 https://www.doi.org/10.33910/2687-153X-2026-7-1-3-15

All heterostructures exhibit a reduced bandgap ($E_g \approx 2.20–2.34$ eV) compared to the pristine $CsPbBr_3$ (2.42 eV). This decrease in E_g is attributed to the formation of additional defect-related and surface states at the ZnO + perovskite interface, which introduce a finite density of states near the band edge and facilitate interband transitions at lower energies, resulting in the observed bathochromic shift (Leelavathi et al. 2013).

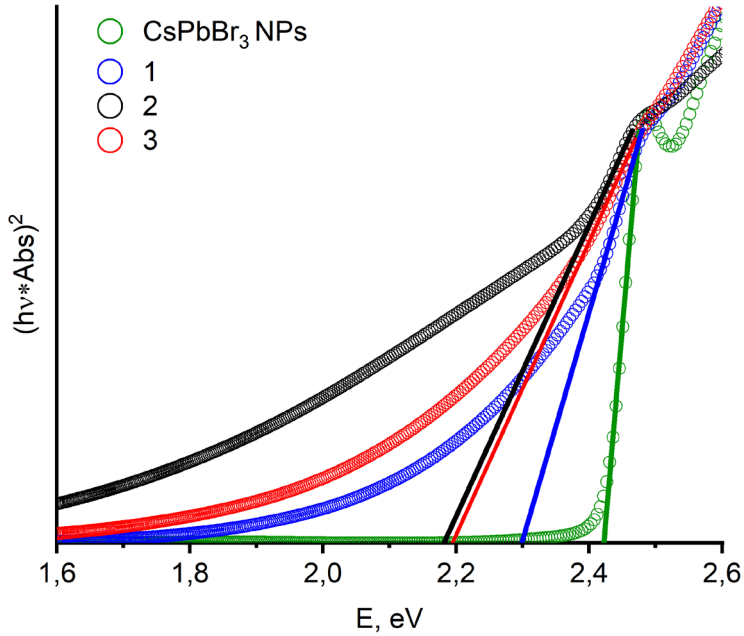

Fig. 4. Normalized absorption spectra of samples near the absorption edge:
1 — H = 1.6 μm; 2 — H = 2.4 μm; 3 — H = 2.7 μm

The most pronounced bathochromic shift and the strongest absorption enhancement are observed for plot 3 (2.7 μm, 50 nm) and plot 2 (2.4 μm, 100 nm), which is attributed to the greater NR height and the more developed interfacial region. These NR arrays provide a larger contact area with the $CsPbBr_3$ layer, including a higher density of grooves, facets, sidewalls, and microscale irregularities capable of hosting the NPs. Collectively, these factors facilitate more efficient modification of the electronic states and enhanced interfacial energy transfer (Leelavathi et al. 2013).

Fig. 5 presents the three-dimensional PL spectra of pristine $CsPbBr_3$ NPs (a) and the ZnO NRs/$CsPbBr_3$ composites with different NR morphologies (b–d). The x-axis corresponds to the photoluminescence wavelength, the y-axis to the PL intensity, and the z-axis to the excitation wavelength, varied from 365 to 400 nm. Pristine $CsPbBr_3$ nanoparticles display an intense and stable emission maximum at ~510 nm for all excitation wavelengths. In the composite samples, a substantial increase in PL intensity is observed, accompanied by a more pronounced dependence on the excitation wavelength: as λ_{exc} increases above ~370 nm, the intensity rises sharply, indicating the involvement of an additional excitation pathway associated with the electronic contribution of the ZnO NRs. In this region, ZnO begins to absorb the excitation light and efficiently transfers energy to the $CsPbBr_3$ NPs through interfacial excited-state transfer processes, leading to enhanced emission from the perovskite NPs (Hasabeldaim et al. 2019; Wu et al. 2005). The magnitude of this enhancement depends on the ZnO NR morphology — specifically their height and diameter — which determines the density of interfacial states and the efficiency of energy transfer, thereby explaining the observed differences among samples 1, 2, and 3.

Fig. 6 shows a projection of the data, equivalent to a rotation of the three-dimensional PL spectra (Fig. 5) such that the excitation wavelength (λ_{exc}) becomes the x-axis, enabling analysis of the evolution of fluorescence as a function of excitation energy. The PL intensity was evaluated at a fixed emission wavelength corresponding to the PL maximum (λ_{em} = 509 nm). The graph reveals that the composite samples exhibit a pronounced increase in intensity within the 370–400 nm region, significantly exceeding the emission levels of the reference $CsPbBr_3$ NPs.

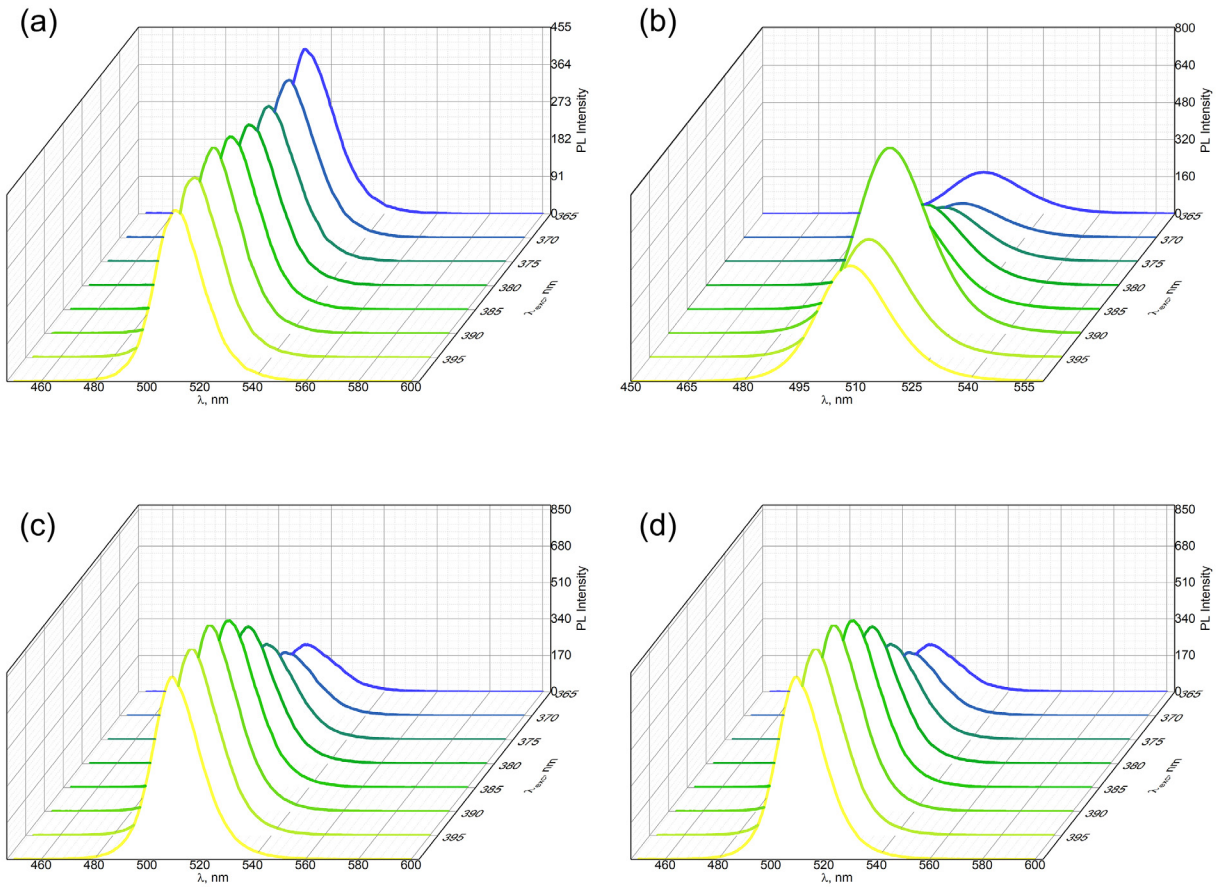

Fig. 5. A series of fluorescence spectra of the samples:
a — $CsPbBr_3$; b — 1 (H = 1.6 μm); c — 2 (H = 2.4 μm); d — 3 (H = 2.7 μm)

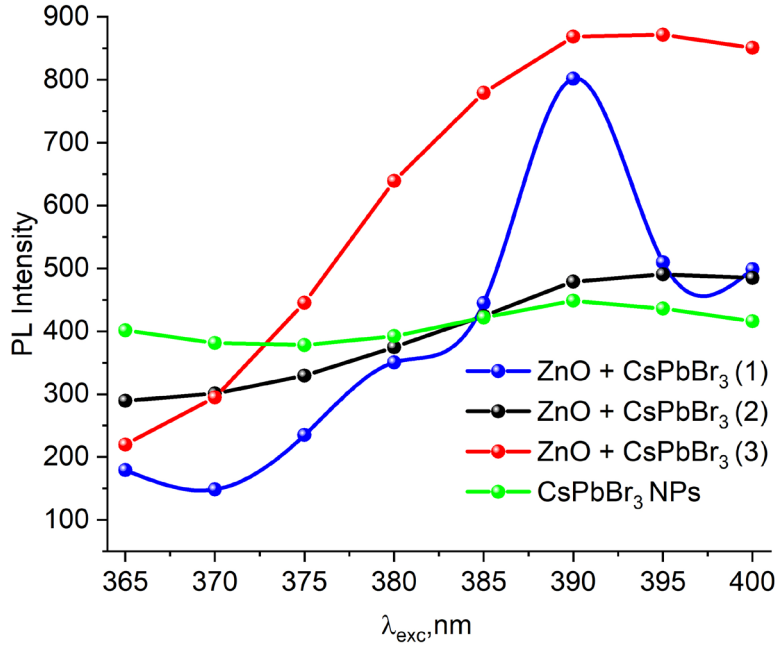

Fig. 6. Dependence of photoluminescence intensity at a fixed emission wavelength of 509 nm on excitation wavelength for ZnO + $CsPbBr_3$ composites and comparison with the reference $CsPbBr_3$: green spectrum — $CsPbBr_3$ NPs; blue — 1 (H = 1.6 μm); black — 2 (H = 2.4 μm); red — 3 (H = 2.7 μm)

https://www.doi.org/10.33910/2687-153X-2026-7-1-3-15

Among the investigated heterostructures, samples 2 (H = 2.4 μm) and 3 (H = 2.7 μm) exhibit the most pronounced and reproducible dependence of photoluminescence intensity on the excitation wavelength. Their spectral profiles are nearly identical in shape, indicating similar mechanisms of interfacial excitation transfer and efficient coupling between the ZnO NRs and the perovskite NPs. Sample 1 (H = 1.6 μm) shows a comparable trend, although its intensity behavior deviates from that of the two selected heterostructures.

Increasing the NR height extends the optical path within the array, enhances light scattering, and promotes deeper penetration of the excitation radiation. These effects raise the probability of ZnO absorption and subsequent energy transfer to $CsPbBr_3$, thereby accounting for the higher photoluminescence observed for the longer NR arrays, such as 2 and 3 (Table 2).

Table 2. Characteristics of the photoluminescence spectra

Sample	$\lambda_{\lambda exc=390\ nm}$, nm	FWHM, nm	Q	Intensity, a.u.	E_g, eV
1	509	23	22.13	802	2.30
2	509.5	20.5	24.85	479	2.18
3	509.5	20.5	24.85	869	2.19
$CsPbBr_3$ NPs	509	21	24.2	448	2.42
ZnO NRs	–	–	–	–	3.22

The same effect plays an important role in the context of SERS. Longer and denser ZnO NRs form a highly developed nanostructured surface with an increased number of electromagnetic 'hot spots,' thereby enhancing local fields and amplifying the Raman response of adsorbed species (Bakry et al. 2024; Korepanov et al. 2019; Thyr et al. 2021). Thus, the morphology that yields higher PL intensity in ZnO + $CsPbBr_3$ heterostructures simultaneously creates favorable conditions for stronger SERS enhancement, as further evidenced by the analysis of the Raman spectra.

In the Raman spectra (Fig. 7) of heterostructures 1, 2, and 3, the $CsPbBr_3$ NPs do not exhibit well-defined vibrational modes. The NPs possess inherently weak Raman activity due to their soft ionic lattice and pronounced anharmonicity, which leads to fluorescence dominating over Raman scattering. In contrast, the ZnO NR substrates display their characteristic phonon modes — E_2 (low) (~99 cm^{-1}), $2E_2$ (~332 cm^{-1}), A_1(TO) (~380 cm^{-1}), and the intense E_2 (high) (~438 cm^{-1}) (Bakry et al. 2024; Korepanov et al. 2019; Thyr et al. 2021).

In the Raman spectra of the ZnO + $CsPbBr_3$ heterostructures, a substantial enhancement of the signal is observed compared to pristine ZnO, indicating the contribution of the perovskite NPs. Additional vibrational features appearing at ~73, 127, 160, and 312 cm^{-1} — identified through multistage Gaussian deconvolution (Fig. 8) — are entirely absent in the spectra of pure ZnO but correspond well to previously reported low-frequency modes of $CsPbBr_3$ (Benadia et al. 2025; Iaru et al. 2021; Li et al. 2021). These modes are typically obscured by strong fluorescence and the inherently weak Raman cross-section of the perovskite; however, in the presence of ZnO NRs, they become enhanced due to local electromagnetic field amplification and the formation of interfacial states at the ZnO + perovskite boundary, consistent with a SERS-like enhancement mechanism.

Conclusions

This work demonstrates that integrating ZnO NRs with $CsPbBr_3$ NPs enables substantial modulation of their optical and vibrational properties through the development of strong interfacial interactions. Analysis of the absorption and photoluminescence spectra revealed that the morphology of the ZnO nanorods — primarily their length — governs the efficiency of energy transfer and the degree of optical enhancement in the hybrid structures. Heterostructures 2 and 3, characterized by greater NR height, exhibit a pronounced bathochromic shift of the absorption edge, the highest PL intensity, and the most favorable conditions for the formation of interfacial electronic states. Raman spectroscopy further confirmed the presence of SERS-like enhancement: in addition to the characteristic ZnO phonon modes, additional low-frequency features corresponding to $CsPbBr_3$ vibrations emerge, enabled

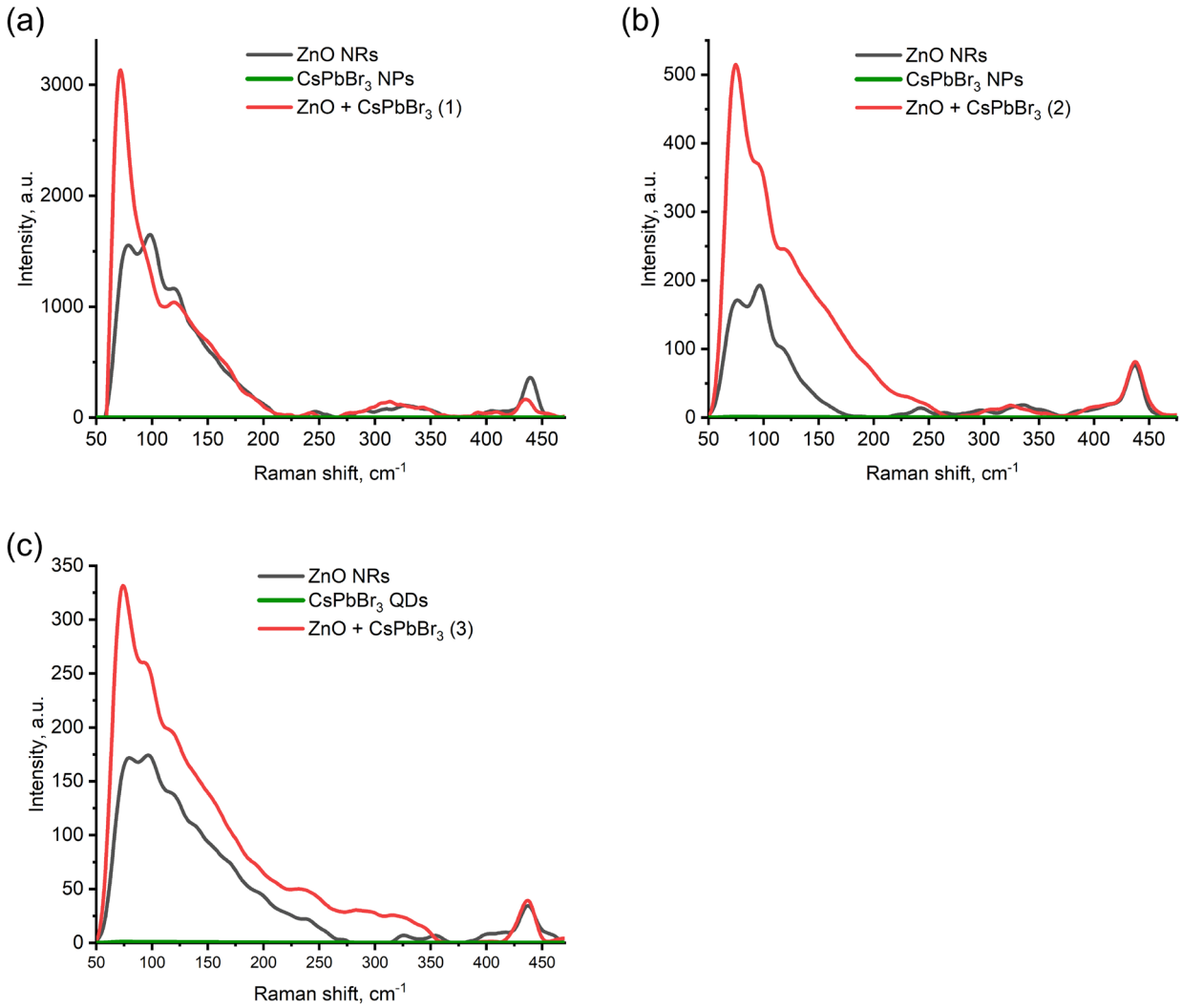

Fig. 7. Raman spectra of heterostructures

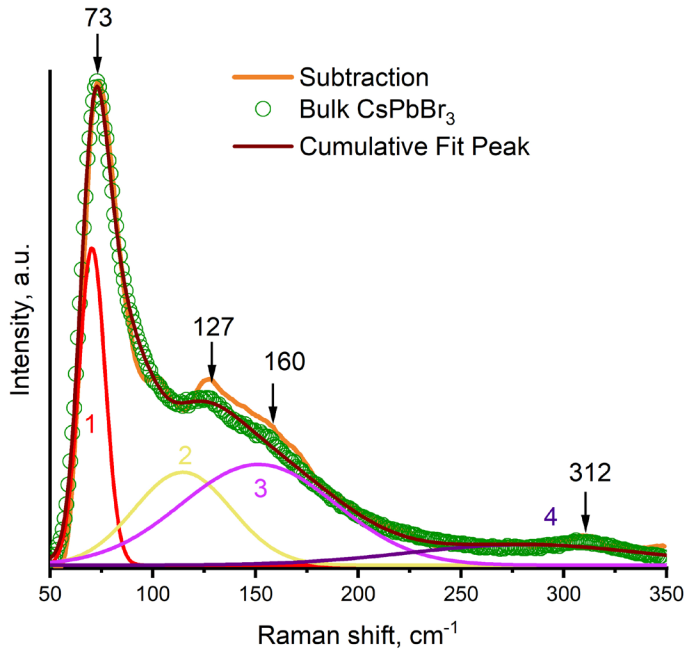

Fig. 8. Revealed low-frequency $CsPbBr_3$ modes enhanced by a ZnO substrate

https://www.doi.org/10.33910/2687-153X-2026-7-1-3-15

by local electromagnetic field amplification and defect-induced interfacial states at the ZnO/perovskite boundary. These findings indicate that ZnO NRs + $CsPbBr_3$ NPs heterostructures represent a promising platform for the development of stable semiconductor-based SERS substrates and hold significant potential for next-generation sensing and optical detection technologies.

Conflict of Interest

The authors declare that there is no conflict of interest, either existing or potential.

Acknowledgements

This research was performed using the equipment of the Joint Research Center of Physical Methods of Research of the Kurnakov Institute of General and Inorganic Chemistry of the Russian Academy of Sciences.

The authors express their deep gratitude to Lydia Sergeevna Volkova, a graduate student at NIU MIET, for her assistance in preparing the manuscript and SEM images of the nanostructures.

Author Contributions

All authors made an equivalent contribution to the preparation of the publication.

References

Ahmed, M. A., Abou-Gamra, Z. M., Alshakhanbeh, M. A. Medien, H. (2019) Control synthesis of metallic gold nanoparticles homogeneously distributed on hexagonal ZnO nanoparticles for photocatalytic degradation of methylene blue dye. *Environmental Nanotechnology, Monitoring & Management*, 12, article 100217. https://doi.org/10.1016/j.enmm.2019.100217 (In English)

Alagurasu, A., Behera, S., Yang, J.-M. et al. (2025) Large-area nanogap platforms for surface-enhanced Raman spectroscopy toward sensing applications: Comparison between Ag and Au. *Biosensors*, 15 (6), article 369. https://doi.org/10.3390/bios15060369 (In English)

Averochkin, E. P., Steparuk, A. S., Teksina, E. V. et al. (2024) Photoactive Layers based on ZnO Nanorods obtained by hydrothermal synthesis for dye-sensitized solar cells. *Russian Journal of Inorganic Chemistry*, 69 (6), 925–932. https://doi.org/10.1134/S0036023624600734 (In English)

Bakry, M., Ismail, W., Abdelfatah, M., El-Shaer, A. (2024) Low-cost fabrication methods of ZnO nanorods and their physical and photoelectrochemical properties for optoelectronic applications. *Scientific Reports*, 14, article 23788. https://doi.org/10.1038/s41598-024-73352-5 (In English)

Benadia, A. G., Pan, L., Bayikadi, K. S. et al. (2025) Progress in solution growth of cuboid $CsPbBr_3$ single crystals with low defect densities and high-sensitivity X-ray detection. *Crystal Growth & Design*, 25 (21), 9288–9299. https://doi.org/10.1021/acs.cgd.5c01107 (In English)

Chiu, Y.-H., Chang, K.-D., Hsu, Y.-J. (2018) Plasmon-mediated charge dynamics and photoactivity enhancement for Au-decorated ZnO nanocrystals. *Journal of Materials Chemistry A*, 6 (10), 4286–4296. https://doi.org/10.1039/C7TA08543E (In English)

Coulter, J. B., Birnie, D. P. III (2018) Degradation mechanism in methylammonium lead iodide perovskite by water: Formation of hydrated HI and PbI2. *Physica Status Solidi B*, 255 (3), article 1700393. https://doi.org/10.1002/pssb.201700393 (In English)

Deng, S., Fan, H. M., Zhang, X. et al. (2009) An effective surface-enhanced Raman scattering template based on a Ag nanocluster–ZnO nanowire array. *Nanotechnology*, 20, article 175705. https://doi.org/10.1088/0957-4484/20/17/175705 (In English)

Djurisic, A. B., Chen, X., Leung, Y. H., Ng, A. M. C. (2012) ZnO nanostructures: Growth, properties and applications. *Journal of Materials Chemistry*, 22, 6526–6535. https://doi.org/10.1039/C2JM15548F (In English)

Dubkov, S. V., Novikov, D. V., Bandarenka, H. V. et al. (2024) Express formation and characterization of SERS-active substrate from a non-degradable Ag-Nb-N-O film. *Applied Surface Science*, 645, article 158682. https://doi.org/10.1016/j.apsusc.2023.158682 (In English)

Gushchina, V. A., Son, A. G., Egorova, A. A. et al. (2024) Synthesis, structures, and optical properties of semiconductor perovskite nanoparticles CsBX3 (B = Pb, Mn; X = Br, Cl). *Russian Journal of Inorganic Chemistry*, 69, 940–948. https://doi.org/10.1134/S0036023624600928 (In English)

Han, X. X., Ji, W., Zhao, B. Ozaki, Y. (2017) Semiconductor-enhanced Raman scattering: active nanomaterials and applications. *Nanoscale*, 9, 4847–4861. https://doi.org/10.1039/C6NR08693D (In English)

Hasabeldaim, E. H. H., Ntwaeaborwa, O. M., Kroon, R. E. et al. (2019) Enhanced green luminescence from ZnO nanorods. *Journal of Vacuum Science & Technology B*, 37 (1), article 011201. https://doi.org/10.1116/1.5052543 (In English)

Iaru, C. M., Brodu, A., van Hoof, N. J. J. et al. (2021) Fröhlich interaction dominated by a single phonon mode in $CsPbBr_3$. *Nature Communications*, 12 (1), article 5844. https://doi.org/10.1038/s41467-021-26192-0 (In English)

Jin, L. She, G., Li, J. et al. (2016) A facile fabrication of Ag-Au-Ag nanostructures with nanogaps for intensified surface-enhanced Raman scattering. *Applied Surface Science*, 389, 67–72. http://dx.doi.org/10.1016/j.apsusc.2016.07.066 (In English)

Kim, K. H., Utashiro, K., Abe, Y., Kawamura, M. (2014) Structural Properties of Zinc Oxide Nanorods Grown on Al-Doped Zinc Oxide Seed Layer and Their Applications in Dye-Sensitized Solar Cells. *Materials*, 7 (4), 2522–2533. https://doi.org/10.3390/ma7042522 (In English)

Kim, S., Jin, J., Kim, Y.-J. et al. (2008) High-harmonic generation by resonant plasmon field enhancement. *Nature*, 453, 757–760. https://doi.org/10.1038/nature07012 (In English)

Korepanov, V. I. Chan, Si-Y., Hsu, H.-C., Hamaguchi, H. (2019) Phonon confinement and size effect in Raman spectra of ZnO nanoparticles. *Heliyon*, 5 (2), article e01222. https://doi.org/10.1016/j.heliyon.2019.e01222 (In English)

Kumar, R., Umar, A., Kumar, G. et al. (2017) Zinc oxide nanostructure-based dye-sensitized solar cells. *Journal of Materials Science*, 52, 4743–4795. https://doi.org/10.1007/s10853-016-0668-z (In English)

Kumar, V., Gupta, R., Bansal, A. (2021) Hydrothermal growth of ZnO nanorods for use in dye-sensitized solar cells. *ACS Applied Nano Materials*, 4, 6212–6222. https://doi.org/10.1021/acsanm.1c01012 (In English)

Lee, S., Cho, S., Jeong, S.-H. et al. (2025) Inverted $CsPbI_3$ perovskite solar cells with all solution processed layers fabricated in high humidity. *Communications Materials*, 6, article 72. https://doi.org/10.1038/s43246-025-00796-1 (In English)

Leelavathi, A., Madrasa, G., Ravishankar, N. (2013) Size-dependent optical properties of ZnO nanocrystals. *Physical Chemistry Chemical Physics*, 15, 10795–10803. https://doi.org/10.1039/C3CP51058A (In English)

Li, S., Yuan, M., Zhuang, W. et al. (2021) Optically-controlled quantum size effect in a hybrid nanocavity composed of a perovskite nanoparticle and a thin gold film. *Laser & Photonics Reviews*, 15 (12), article 2000480. https://doi.org/10.1002/lpor.202000480 (In English)

Majee, B. P., Bhawna, Mishra, A. K. (2020) Bi-functional ZnO nanoparticles as a reusable SERS substrate for nanomolar detection of organic pollutants. *Materials Research Express*, 6, article 1250j1. https://doi.org/10.1088/2053-1591/ab6f31 (In English)

Majumdar, D. (2024) 2D material-based surface-enhanced Raman spectroscopy platforms (either alone or in nanocomposite form)-from a chemical enhancement perspective. *ACS Omega*, 9 (38), 40242–40258. https://doi.org/10.1021/acsomega.4c06398 (In English)

Miao, J., Liu, Y., Xiao, Y. et al. (2025) Water-stable perovskite/metallic nanocomposites-based SERS aptasensor for detection of neuron-specific enolase. *Biosensors and Bioelectronics*, 280, article 117462. https://doi.org/10.1016/j.bios.2025.117462 (In English)

Novikov, D. V., Malakhov, N. S, Tarasov, A. M. et al. (2021) Development of self-cleaning SERS-active nanostructures based on ZnO nanorods and Ag nanoparticles. *Journal of Physics: Conference Series*, 2103, article 012128. https://doi.org/10.1088/1742-6596/2103/1/012128 (In English)

Peng, Y., Jiang, D., Zhao, M. et al. (2023) High-performance UV–visible photodetectors based on ZnO/perovskite heterostructures. *Journal of Alloys and Compounds*, 965, article 171372. https://doi.org/10.1016/j.jallcom.2023.171372 (In English)

Salem, M., Amor, O., Haouas, A. et al. (2025) Improved optoelectronic efficiency of $CsPbBr_3$ perovskite thin films decorated by ZnO nanoparticles. *Optical and Quantum Electronics*, 57, article 446. https://doi.org/10.1007/s11082-025-08383-x (In English)

Samanta, P. K., Bandyopadhyay, A. K. (2012) Chemical growth of hexagonal zinc oxide nanorods and their optical properties. *Applied Nanoscience*, 2, 111–117. https://doi.org/10.1007/s13204-011-0038-8 (In English)

Saran, R., Heuer-Jungemann, A., Kanaras, A. G., Curry, R. J. (2017) Giant bandgap renormalization and exciton–phonon scattering in perovskite nanocrystals. *Advanced Optical Materials*, 5 (17), article 1700231. https://doi.org/10.1002/adom.201700231 (In English)

Shah, M. A. (2008) Zinc oxide nanorods prepared at low temperatures without catalyst. *Modern Physics Letters B*, 22 (26), 2617–2621. https://doi.org/10.1142/S0217984908017126 (In English)

Sharma, B., Frontiera, R. R., Henry, A.-I. (2012) SERS: Materials, applications, and the future. *Materials Today*, 15 (1–2), 16–25. https://doi.org/10.1016/S1369-7021(12)70017-2 (In English)

Sinha, G., Depero, L. E., Alessandri, I. (2011) Recyclable SERS substrates based on Au-Coated ZnO nanorods. *ACS Applied Materials & Interfaces*, 3 (7), 2557–2563. https://doi.org/10.1021/am200396n (In English)

Song, G., Cong, S. Zhao, Z. (2022) Defect engineering in semiconductor-based SERS. *Chemical Science*, 13 (5), 1210–1224. https://doi.org/10.1039/D1SC05940H (In English)

Tauc, J., Scott, T. A. (1967) Direct determination of optical absorption edge in amorphous semiconductors. *Physics Today*, 20 (10), 105–116. https://doi.org/10.1063/1.3033945 (In English)

Thyr, J., Osterlund, L., Edvinsson, T. (2021) Polarized and non-polarized Raman spectroscopy of ZnO crystals: Method for determination of crystal growth and crystal plane orientation for nanomaterials. *Journal of Raman Spectroscopy*, 52 (8), 1395–1405. https://doi.org/10.1002/jrs.6148 (In English)

Toma, F. T. Z., Rahman, M. S., Maria, K. H. (2025) A review of recent advances in ZnO nanostructured thin films by various deposition techniques. *Discover Materials*, 5, 60. https://doi.org/10.1007/s43939-025-00201-1 (In English)

Vo-Dinh, T., Liu, Y., Fales, A. M. et al. (2015) SERS nanosensors and nanoreporters: Golden opportunities in biomedical applications. *WIREs Nanomedicine and Nanobiotechnology*, 7 (1), 17–33. https://doi.org/10.1002/wnan.1283 (In English)

Wang, H., Zhang, P., Zang, Z. (2020) High performance $CsPbBr_3$ quantum dots photodetectors by using zinc oxide nanorods arrays as an electron-transport layer. *Applied Physics Letters*, 116, 162103. https://doi.org/10.1063/5.0005464 (In English)

Wang, J., Zou, L., Yang, M. et al. (2023) Improvement of the stability and optical properties of $CsPbBr_3$ QDs. *Nanomaterials*, 13 (16), article 2372. https://doi.org/10.3390/nano13162372 (In English)

Wang, X., Chen, Y., Zhang, W. et al. (2025) Highly sensitive and reproducible SERS substrates based on a novel 3D waffle-like PMMA–$CsPbBr_3$–Au ternary film. *Sensors and Actuators B: Chemical*, 431, article 137434. https://doi.org/10.1016/j.snb.2025.137434 (In English)

Wu, L., Wu, Y, Lu, W. (2005) Preparation of ZnO Nanorods and optical characterizations. *Physica E*, 28 (1), 76–82. https://doi.org/10.1016/j.physe.2005.02.005 (In English)

Wu, T., Wang, A., Zheng, L. et al. (2019) Evolution of native defects in ZnO nanorods irradiated with hydrogen ion. *Scientific Reports*, 9, article 17393. https://doi.org/10.1038/s41598-019-53951-3 (In English)

Xia, L., Chen, M., Zhao, X. et al. (2014) Visualized method of chemical enhancement mechanism on SERS and TERS. *Journal of Raman Spectroscopy*, 45 (6), 524–530. https://doi.org/10.1002/jrs.4504 (In English)

Xu, Y., Aljuhani, W., Zhang, Y. et al. (2025) A practical approach to quantitative analytical surface-enhanced Raman spectroscopy. *Chemical Society Reviews*, 54 (1), 62–84. https://doi.org/10.1039/D4CS00861H (In English)

Yi, J., You, E. M., Hu, R. et al. (2025) Surface-enhanced Raman spectroscopy: a half-century historical perspective. *Chemical Society Reviews*, 54 (3), article 1453. https://doi.org/10.1039/D4CS00883A (In English)

Zhao, Y., Xu, Y., Jing, X., Ma, W. (2023) SERS-active plasmonic metal NP-$CsPbX_3$ films for multiple veterinary drug residues detection. *Food Chemistry*, 412, article 135420. https://doi.org/10.1016/j.foodchem.2023.135420 (In English)

Zhou, J., Du, Z., Xie, B., Wang, B. (2025) Potential-controlled interfacial charge transfer and chemical enhancement of SERS spectra in plasmonic molecular junctions. *Journal of Physical Chemistry C*, 129 (7), 3646–3652. https://doi.org/10.1021/acs.jpcc.4c07711 (In English)